RSC Advances

PAPER

View Article Online
View Journal | View Issue

Cite this: RSC Adv., 2017, 7, 27235

Surfactant-assisted solid-state synthesis of $6LiMn_{0.8}Fe_{0.2}PO_4 \cdot Li_3V_2(PO_4)_3/C$ nanocomposite for lithium-ion batteries

Yanming Wang,[ab] Bo Zhu,[a] Xiaoyu Liu[a] and Fei Wang *[ab]

Received 22nd March 2017
Accepted 4th May 2017

DOI: 10.1039/c7ra03337k

rsc.li/rsc-advances

Herein, nanosized $LiMnPO_4/C$, $LiMn_{0.8}Fe_{0.2}PO_4/C$, and $6LiMn_{0.8}Fe_{0.2}PO_4 \cdot Li_3V_2(PO_4)_3/C$ cathode materials were synthesized by a facile surfactant-assisted solid-state method. Lauric acid was used as a surfactant and carbon source to fabricate the carbon-coated nanoparticles. The phase compositions and elemental distribution of $6LiMn_{0.8}Fe_{0.2}PO_4 \cdot Li_3V_2(PO_4)_3/C$ were analyzed *via* X-ray diffraction and energy dispersive spectroscopy. Due to the unique heterogeneous nanostructure, $6LiMn_{0.8}Fe_{0.2}PO_4 \cdot Li_3V_2(PO_4)_3/C$ exhibits superior electrochemical performance as compared to the individual $LiMn_{0.8}Fe_{0.2}PO_4/C$ and $LiMnPO_4/C$. The composite cathode delivers large discharge capacities of 162 and 167 mA h g^{-1} at 0.1C in the voltage range of 2.0–4.5 V and 2.0–4.8 V, respectively, along with good rate capability and long cycle life.

1. Introduction

During the recent decade, the rapidly developing electric vehicles and hybrid electric vehicles urgently need safe lithium-ion batteries as a driving power source. Compared to commercial metal-oxide cathode materials, polyanionic $LiMPO_4$ (M = Fe, Mn, and Co) cathodes exhibit superior structural and thermal stability due to the existence of strong covalent P–O bonds.[1,2] $LiMnPO_4$ shows great potential for application in power batteries owing to the virtues of large theoretical capacity (171 mA h g^{-1}), high discharge voltage (4.1 V *vs.* Li/Li^+), and an abundant manganese source.[3] However, the low electronic conductivity of $LiMnPO_4$ ($<10^{-10}$ S cm^{-1}) restricts its reversible capacity at high currents.[4]

Recent reports have proven that the electrochemical kinetics of $LiMnPO_4$ can be remarkably improved by partially replacing Mn with Fe.[5–26] Various $LiMn_{1-y}Fe_yPO_4$ ($0 < y < 1$) solid solutions, such as $LiMn_{0.9}Fe_{0.1}PO_4$,[11,12] $LiMn_{0.8}Fe_{0.2}PO_4$,[13–16] $LiMn_{0.6}Fe_{0.4}PO_4$,[17–19] $LiMn_{0.5}Fe_{0.5}PO_4$,[20] $LiMn_{0.4}Fe_{0.6}PO_4$,[21–23] *etc.*, exhibit much better electrochemical performance than the pristine $LiMnPO_4$. Yang *et al.*[24] synthesized a $LiMn_{0.8}Fe_{0.2}PO_4/C$ composite using a co-precipitation method, which provided a specific capacity of 160.6 mA h g^{-1} at 0.05C. Xiang *et al.*[25] reported the template-engaged synthesis of $LiMn_{0.5}Fe_{0.5}PO_4/C$ porous spheres, and the spheres exhibited capacity retention of 90.7% over 100 cycles at 1C. In general, the reversible capacity of $LiFe_yMn_{1-y}PO_4$ increases with an increase in the Fe content. However, high Fe content reduces the energy density of $LiFe_yMn_{1-y}PO_4$ due to the relatively low redox potential of Fe^{3+}/Fe^{2+} (3.5 V *vs.* Li/Li^+). More recently, the reported multiphase composites of $xLiFePO_4 \cdot yLi_3V_2(PO_4)_3$ and $xLiMnPO_4 \cdot yLi_3V_2(PO_4)_3$ presented superior rate capability than individual $LiFePO_4$ and $LiMnPO_4$, respectively.[26–30] The electrochemical activity of $LiFePO_4$ and $LiMnPO_4$ can be obviously enhanced by blending with the fast ion conductor $Li_3V_2(PO_4)_3$.[31–33] For example, Qin *et al.*[34] prepared $(1-x)LiMnPO_4 \cdot xLi_3V_2(PO_4)_3/C$ composites through a solid-state method, and $0.6LiMnPO_4 \cdot 0.4Li_3V_2(PO_4)_3/C$ showed much larger capacity of 130 mA h g^{-1} at 0.1C than 76 mA h g^{-1} of pristine $LiMnPO_4/C$. According to the abovementioned studies, a novel strategy of combining the advantages of a solid solution and multiphase composite was proposed to prepare high-performance $LiMnPO_4$-based composite cathode materials.[35] Wu *et al.*[36] reported the synthesis of $5LiMn_{0.9}Fe_{0.1}PO_4 \cdot Li_3V_2(PO_4)_3/C$, which showed satisfactory performance with the specific capacity of 158 mA h g^{-1} at 0.05C as compared to 70 mA h g^{-1} of $LiMn_{0.9}Fe_{0.1}PO_4/C$. Although $Li_3V_2(PO_4)_3$ is a fast rate cathode for rechargeable lithium batteries, the theoretical capacity of 133 mA h g^{-1} while charging to 4.3 V is relatively lower. Furthermore, the cost of V is much higher than that of Mn or Fe; thus, the high cost of $Li_3V_2(PO_4)_3$ restricts its large-scale application in power batteries. Based on the cost and performance of the cathode material, $LiMn_{1-y}Fe_yPO_4$ incorporated with a small quantity of $Li_3V_2(PO_4)_3$ may be a feasible choice.

The simple solid-state reaction method has been widely employed in industry to prepare various cathode materials for lithium batteries. However, the nanoparticles tend to aggregate and grow further during the high-temperature calcination. The big particle size usually causes slow lithium ion diffusion in the polyanionic cathode materials. To synthesize high dispersing nanoparticles using a solid-state reaction, several surfactants,

---

[a] *Anhui Key Laboratory of Energetic Materials, School of Chemistry and Materials Science, Huaibei Normal University, Huaibei, Anhui 235000, China. E-mail: wangfeichem@126.com; Fax: +86 561 3806281; Tel: +86 561 3802235*

[b] *Information College, Huaibei Normal University, Huaibei, Anhui 235000, China*

such as oleic acid,[37,38] poly(acrylic acid),[39] Tween,[40] Span,[41] *etc.*, have been introduced to suppress the particle growth and aggregation. In this study, we described a facile solid-state synthesis of $6LiMn_{0.8}Fe_{0.2}PO_4 \cdot Li_3V_2(PO_4)_3/C$ nanocomposites using lauric acid as a surfactant and carbon source. Moreover, physical characterization and electrochemical properties of $6LiMn_{0.8}Fe_{0.2}PO_4 \cdot Li_3V_2(PO_4)_3/C$ were studied in detail.

2. Experimental

Stoichiometric amounts of Li_2CO_3, $Mn(CH_3COO)_2 \cdot 4H_2O$, FeC_2O_4, NH_4VO_3, $NH_4H_2PO_4$, and lauric acid were mixed with ethanol media and ball-milled in a zirconia container at 400 rpm for 5 h. The molar ratio of Li/lauric acid was 1 : 2.5. The obtained precursor mixture was pre-decomposed at 350 °C for 4 h and subsequently heated at 700 °C under an Ar/H_2 atmosphere (7% H_2) for 10 h to yield the $6LiMn_{0.8}Fe_{0.2}PO_4 \cdot Li_3V_2(PO_4)_3/C$ composite. For comparison, the $LiMnPO_4/C$ and $LiMn_{0.8}Fe_{0.2}PO_4/C$ composites were synthesized in a similar manner. $LiMnPO_4/C$, $LiMn_{0.8}Fe_{0.2}PO_4/C$, and $6LiMn_{0.8}Fe_{0.2}PO_4 \cdot Li_3V_2(PO_4)_3/C$ have been abbreviated as LMP/C, LMFP/C, and 6LMFP·LVP/C, respectively.

The phase structure was determined using a powder X-ray diffractometer (XRD, Rigaku D/max-2550VL/PC, Cu Kα radiation), operating at 40 kV and 200 mA. The morphology, carbon layer, and elemental distribution of the as-synthesized composites were characterized by scanning electron microscopy (SEM, Hitachi-SU8020) and high-resolution transmission electron microscopy (HRTEM, JEOL-2100F) equipped with an energy dispersive X-ray spectroscopy (EDS). The carbon amounts of all the composites were evaluated by an elemental analyzer (Vario EL Cube). The chemical composition of the cathode material was analyzed *via* inductively coupled plasma atomic emission spectroscopy (ICP, iCAP 7600).

The electrochemical properties of the LMP/C, LMFP/C, and 6LMFP·LVP/C composites were studied using coin cells with lithium-foil as the anode and Entek ET20-26 membrane as the separator. The cathode consisted of 80 wt% active composite, 10 wt% Super P conducting carbon, and 10 wt% poly(vinylidene fluoride). A 1 M solution of $LiPF_6$ in the mixed solvents of ethylene carbonate and dimethyl carbonate (1 : 1, v/v) acted as the electrolyte. The charge–discharge measurements were performed using a battery testing system (LANHE CT2001) in the voltage range of 2.0–4.5 V and 2.0–4.8 V, respectively. The elevated temperature performance of 6LMFP·LVP/C was also determined at 50 °C. The cyclic voltammogram (CV) and electrochemical impedance spectra (EIS) were obtained using an electrochemical analyzer (CHI 650D).

3. Results and discussion

Fig. 1 presents the XRD patterns of the as-synthesized composites and Rietveld refinement of 6LMFP·LVP/C. The sharp diffraction peaks of LMP/C can be fully assigned to the olivine-type crystal structure with the *Pnmb* space group (JCPDS no. 74-0375). Moreover, the diffraction peaks of LMFP/C are similar to those of LMP/C without any indefinite peak, indicating the pure solid solution phase of $LiMn_{0.8}Fe_{0.2}PO_4$. Both the $LiMn_{0.8}Fe_{0.2}PO_4$ and $Li_3V_2(PO_4)_3$ phases were observed in the 6LMFP·LVP/C composite with a small unidentified phase at 28.3°. The diffraction peaks of LMFP/C and 6LMFP·LVP/C slightly shifted to higher 2θ angles relative to those of LMP/C, which may be attributed to the smaller ionic radius of Fe^{2+} (0.78 Å) and V^{3+} (0.74 Å) than that of Mn^{2+} (0.80 Å). The lattice parameters of the olivine phase in LMP/C, LMFP/C, and 6LMFP·LVP/C composites, analyzed *via* Rietveld refinement, are compared in Table 1. The cell volume of $LiMnPO_4$ decreases when Fe is introduced, and it further decreases when $Li_3V_2(PO_4)_3$ is incorporated, which indicates that some Fe and V diffuse into the $LiMnPO_4$ host lattice. Previous studies have revealed that doping $LiMnPO_4$ with Fe^{2+} and V^{3+} could improve the electronic and electrochemical kinetics.[5,31,32]

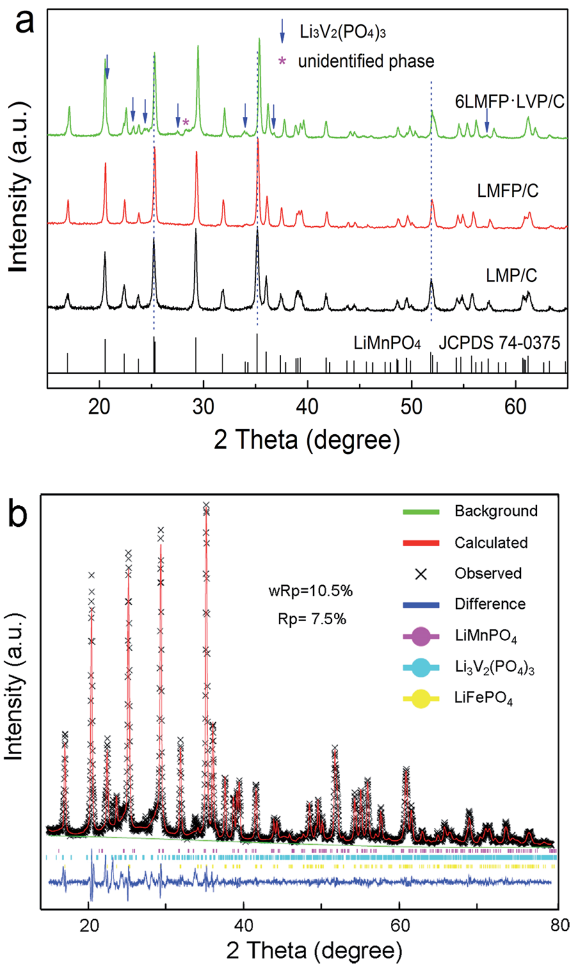

Fig. 1 XRD patterns of the as-synthesized composites (a) and Rietveld refinement of 6LMFP·LVP/C (b).

Table 1 Lattice parameters of the olivine phase in the composites

Sample	*a* (Å)	*b* (Å)	*c* (Å)	Volume (Å^3)
LMP	6.0942	10.4358	4.7487	302.01
LMFP	6.0671	10.4262	4.7358	299.57
6LMFP·LVP	6.0558	10.4168	4.7273	298.21

Fig. 2a–c show the SEM images of the LMP/C, LMFP/C, and 6LMFP·LVP/C powders. All the samples illustrate similar nanoparticles morphology with the size of *ca.* 100–150 nm and narrow distribution. The TEM images (Fig. 2d and e) exhibit that the well-dispersed 6LMFP·LVP/C granules are interconnected by the amorphous carbon layer rather than agglomerated into larger blocks. A homogenous carbon layer formed from the pyrolysis of lauric acid is tightly coated on the surface of the 6LMFP·LVP nanoparticles in a thickness of *ca.* 3 nm. The carbon contents evaluated by elemental analysis are

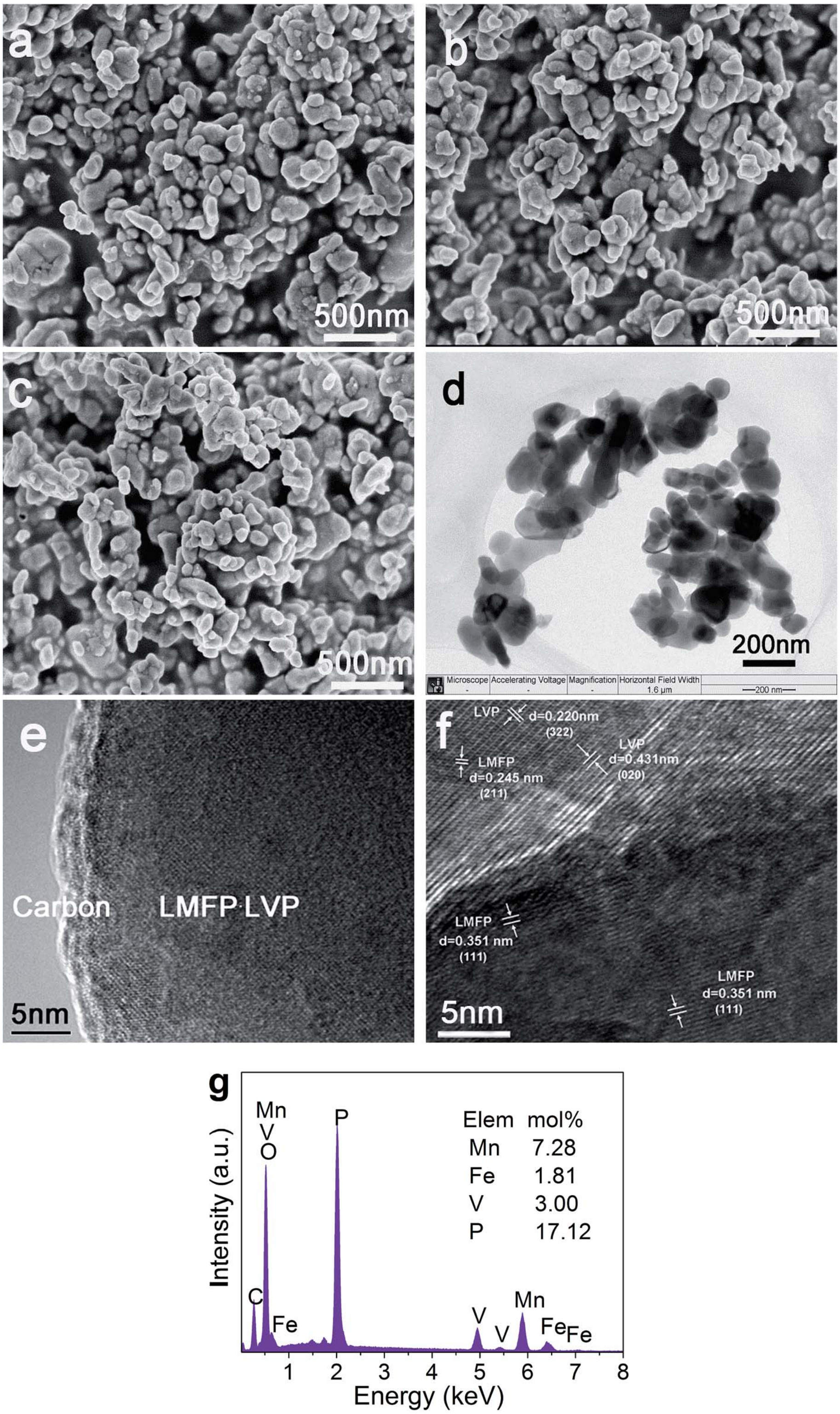

Fig. 2 SEM images of LMP/C (a), LMFP/C (b), and 6LMFP·LVP/C (c); TEM images (d and e), HRTEM image (f), and EDS pattern (g) of 6LMFP·LVP/C.

6.27 wt%, 6.32 wt%, and 6.43 wt% for the LMP/C, LMFP/C, and 6LMFP·LVP/C powders, respectively. The phase compositions of 6LMFP·LVP/C are indicated in the HRTEM image (Fig. 2f). The interplanar spacing of 0.351 and 0.245 nm correspond to the (111) and (211) planes of $LiMn_{0.8}Fe_{0.2}PO_4$, whereas the interplanar spacing of 0.431 nm and 0.220 are attributed to the (020) and (322) planes of $Li_3V_2(PO_4)_3$. The results imply that both $LiMn_{0.8}Fe_{0.2}PO_4$ and $Li_3V_2(PO_4)_3$ phases coexist in the 6LMFP·LVP/C composite particles. The EDS spectrum of 6LMFP·LVP/C (Fig. 2g) displays the characteristic peaks of Mn, Fe, V, P, O, and C. The molar ratio of Mn : Fe : V is 7.28 : 1.81 : 3.00, which is basically in accordance with the theoretical ratio of 2.4 : 0.6 : 1. The chemical composition of 6LMFP·LVP/C was further measured by ICP and is listed in Table 2.

Fig. 3 illustrates the formation procedure of 6LMFP·LVP/C. Lauric acid ($CH_3(CH_2)_{10}COOH$) is a saturated fatty acid with a relatively low melting point of 44 °C. During the heating process, lauric acid can form a molten media in which the carboxylic groups of lauric acid conjugate the inorganic cations and the long carbon chains separate the precursors. Thus, the 6LMFP·LVP crystallites can grow in a confined environment. Moreover, the crystallites are enveloped in an *in situ* conductive carbon layer generated from the decomposition of lauric acid. This effectively restrains the aggregation of the nanoparticles and further growth. Lauric acid, acted as a surfactant and carbon source, is favorable for fabricating granular nanocomposites with good dispersion. The distribution of the elements in 6LMFP·LVP/C was characterized by EDS. As shown in Fig. 4, the elements Mn, Fe, V, and P are homogeneously dispersed in every 6LMFP·LVP/C nanoparticle, such as a particle marked as A. The EDS mappings, together with HRTEM image (Fig. 2f), indicate that the $Li_3V_2(PO_4)_3$ phase uniformly diffuses into the $LiMn_{0.8}Fe_{0.2}PO_4$ matrix, forming a multiphase dispersoid rather than existing as individual $LiMn_{0.8}Fe_{0.2}PO_4$ and $Li_3V_2(PO_4)_3$ particles.

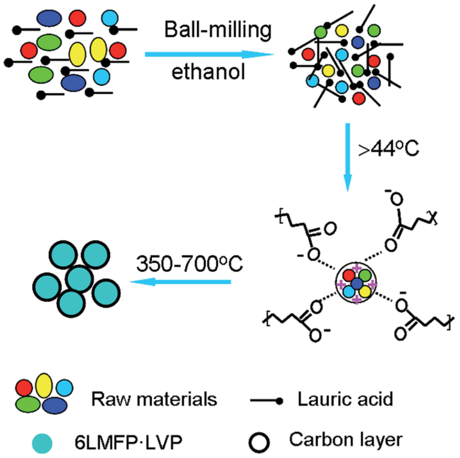

Fig. 3 Schematic of the synthesis of carbon-coated 6LMFP·LVP.

Fig. 5a shows the initial charge–discharge curves of the LMP/C, LMFP/C, and 6LMFP·LVP/C composites. The cells were charged to 4.5 V at 0.1C rate (17 mA g^{-1}), kept at 4.5 V until the current decreased to 0.02C, and then discharged to 2.0 V at 0.1C rate. As observed for LMP/C, a pair of sloping voltage plateaus (4.22/3.93 V) corresponds to the phase transition of $LiMnPO_4 \leftrightarrow MnPO_4$.[1,2] Compared with LMP/C, LMFP/C presents another pair of voltage plateaus (3.62/3.58 V), associating with the phase transition of $LiFePO_4 \leftrightarrow FePO_4$.[9,10] For the 6LMFP·LVP/C sample, three pairs of voltage plateaus (3.59/3.58, 3.68/3.66, 4.08/4.02 V) are assigned to the sequential phase transitions of $Li_3V_2(PO_4)_3 \leftrightarrow Li_{2.5}V_2(PO_4)_3 \leftrightarrow Li_2V_2(PO_4)_3 \leftrightarrow LiV_2(PO_4)_3$,[32,36,42] respectively. However, the charge plateau of Fe^{3+}/Fe^{2+} is invisible because of overlapping with the plateau of $Li_xV_2(PO_4)_3$ (x from 3 to 2.5). Note that the voltage difference between the charge and discharge plateaus corresponding to $LiMnPO_4 \leftrightarrow MnPO_4$ decreases when Fe is introduced and further decreases when $Li_3V_2(PO_4)_3$ is introduced, demonstrating smaller polarization and higher electrochemical kinetics. Moreover, the initial discharge capacity reaches 162 mA h g^{-1} for the 6LMFP·LVP/C sample at 0.1C rate, whereas it reaches 144 mA h g^{-1} for LMFP/C and 124 mA h g^{-1} for LMP/C under the same conditions.

Table 2 Molar ratio of the prepared 6LMFP·LVP/C measured by ICP

	Molar ratio	
Element	Theoretical	6LMFP·LVP/C
Li	4.5	4.63
Mn	2.4	2.43
Fe	0.6	0.58
V	1	1
P	4.5	4.42

Fig. 5b exhibits the rate capabilities of the LMP/C, LMFP/C, and 6LMFP·LVP/C composites. Obviously, the rate capability of 6LMFP·LVP/C is superior to those of LMFP/C and LMP/C. The discharge capacities of 6LMFP·LVP/C at 0.5, 1, and 2C rates are 150, 146, and 139 mA h g^{-1}, compared to 133, 125, and 111 mA h g^{-1} for LMFP/C and 111, 102, and 92 mA h g^{-1} for LMP/C. Even at 5C, a higher discharge capacity of 128 mA h g^{-1} for 6LMFP·LVP/C was achieved. The rate performance of the as-prepared 6LMFP·LVP/C nanocomposite exceeded those of the reported $LiMn_{0.8}Fe_{0.2}PO_4/C$,[13] $0.5LiMnPO_4\cdot 0.5\ Li_3V_2(PO_4)_3/C$,[30] $5LiMn_{0.9}Fe_{0.1}PO_4\cdot Li_3V_2(PO_4)_3/C$ (ref. 36), and $0.95LiMn_{0.95}Fe_{0.05}PO_4\cdot 0.05Li_3V_2(PO_4)_3/C$ (ref. 35) composites. The cycling stabilities of LMP/C, LMFP/C, and 6LMFP·LVP/C were characterized at 0.5C after the rate capability test. It can be observed that the discharge capacities of these composites decrease with the increasing C-rate. More importantly, when the discharge rate returns to 0.5C after testing at 5C, the capacities of three composites resumed the former state and faded less than 5% after subsequent 100 cycles, implying high electrochemical reversibility and structural stability for all the samples. The superior high-rate performance of 6LMFP·LVP/C could be attributed to its unique heterogeneous nanostructures. First, the collaborative effect of Fe and V co-doping and the complete conductive carbon coating effectively promote the electrical conductivity in the bulk phase and at the surface, respectively.[3] Second, the dispersion of $Li_3V_2(PO_4)_3$ crystallites in the

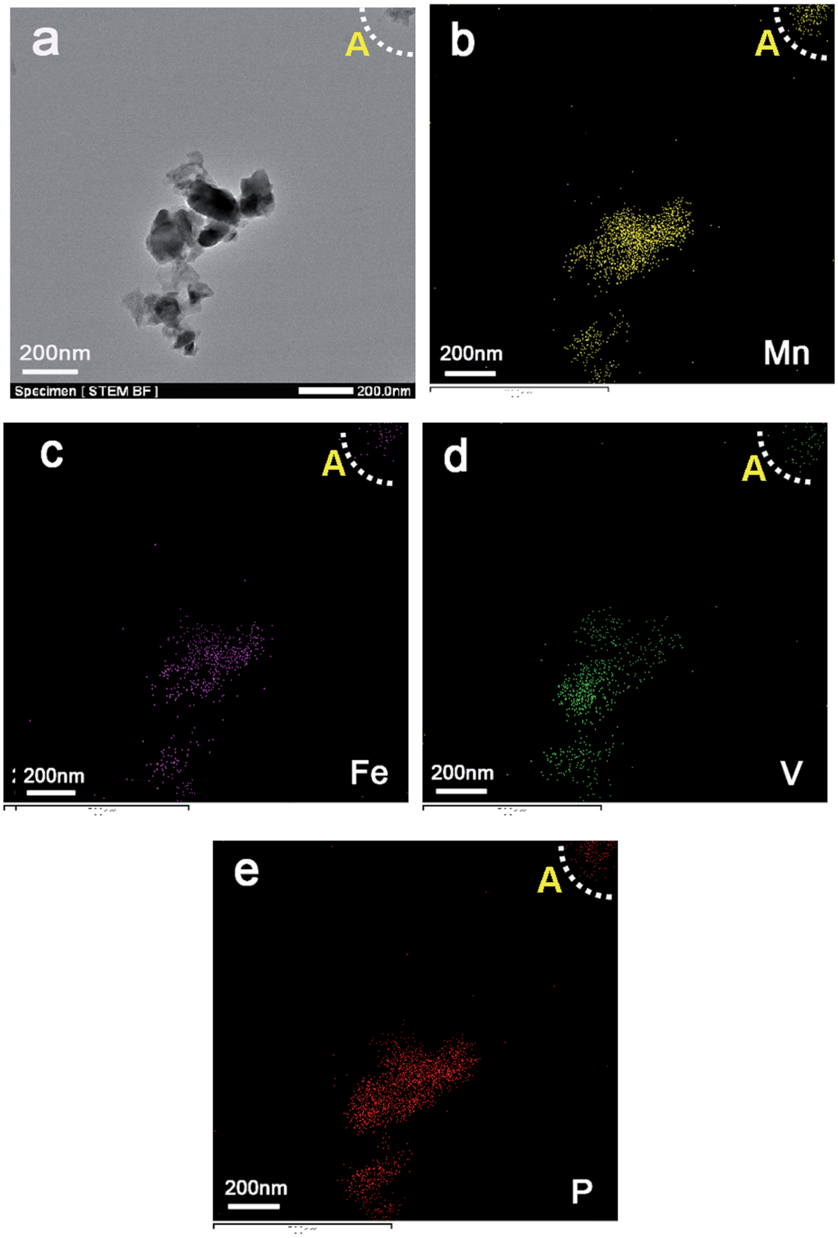

Fig. 4 EDS mappings of 6LMFP·LVP/C for Mn, Fe, V, and P.

$LiMn_{0.8}Fe_{0.2}PO_4$ matrix reduces the Li^+ diffusion pathway in bulk $LiMnPO_4$, which facilitates faster Li-ion intercalation kinetics.

The electrochemical performance of the 6LMFP·LVP/C composite cycled in a wide voltage range of 2.0–4.8 V was also been investigated. Fig. 6a displays the typical charge–discharge curves of 6LMFP·LVP/C at 0.1C and 0.5C. When the end-of-charge voltage extended to 4.8 V, another plateau at 4.52 V in the charge curve was observed, which belonged to the extraction of the third Li^+ from $Li_3V_2(PO_4)_3$. The charge and discharge capacities of 6LMFP·LVP/C at the second cycle are 178 and 167 mA h g^{-1} at 0.1C rate, respectively, with the corresponding coulombic efficiency of 93.8%. At a 0.5C rate, a discharge capacity of 143 mA h g^{-1} was still achieved, and the capacity retention was as high as 91% at the end of 250 cycles. The slight capacity loss may be induced by the deterioration of the electrode/electrolyte interface, resulting from the electrolyte decomposition at high potential.

Fig. 7 describes the charge–discharge curve and cycle life (inset) of 6LMFP·LVP/C at 50 °C. In comparison with the charge–discharge curve obtained at room temperature, as shown in Fig. 5a, 6LMFP·LVP/C presents smaller hysteresis between charge and discharge and flatter charge plateau of Mn^{3+}/Mn^{2+} at elevated temperature. Furthermore, the charge plateaus of Fe^{3+}/Fe^{2+} (3.55 V) and V^{5+}/V^{4+} (4.47 V) can be distinctly observed, demonstrating its improved electrode kinetics at high temperature. The 6LMFP·LVP/C delivers

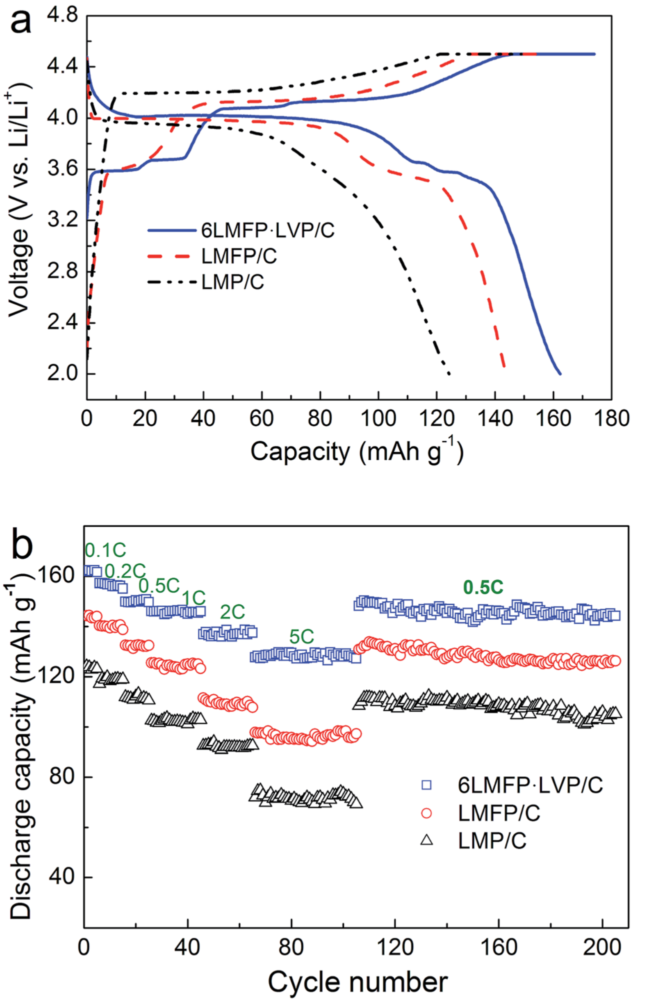

Fig. 5 Charge–discharge curves at 0.1C rate (a) and rate capabilities (b) of LMP/C, LMFP/C and 6LMFP·LVP/C.

a large reversible capacity of 154 mA h g^{-1} at 1C rate and provides a capacity retention of about 90% over 100 cycles, illustrating a good high-temperature stability of the electrode.

To further clarify the synergistic effects of the solid solution and multiphase composition, cyclic voltammetry was employed to analyze the lithiation/delithiation behavior. Fig. 8 compares the CV curves of LMP/C, LMFP/C, and 6LMFP·LVP/C electrodes at a scan speed of 0.1 mV s^{-1}. One couple peak located at 3.68/3.51 V for LMFP/C and three couple peaks located at 3.62/3.57, 3.70/3.65, and 4.11/4.04 V for 6LMFP·LVP/C are ascribed to the redox of Fe^{3+}/Fe^{2+} and V^{4+}/V^{3+}, respectively. The peak couples at 4.33/3.92 for LMP/C, 4.23/3.92 for LMFP/C, and 4.20/3.95 V for 6LMFP·LVP/C are associated with the redox of Mn^{3+}/Mn^{2+}. More significantly, the separation potentials between the Mn^{3+}/Mn^{2+} redox peaks decrease from 0.41 V of LMP/C to 0.31 V of LMFP/C and 0.25 V of 6LMFP·LVP/C. The abovementioned results are in accordance with the charge–discharge curves, which suggest that the electrochemical activity of $LiMnPO_4$ is remarkably enhanced by the appropriate Fe substitution and combination of $Li_3V_2(PO_4)_3$.

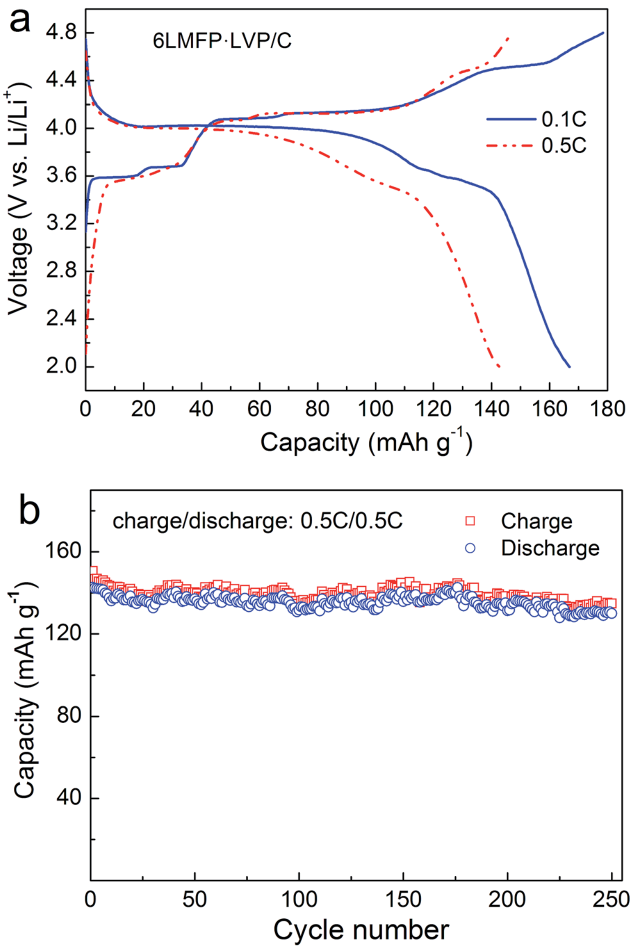

Fig. 6 Charge–discharge curves (a) and cycling performance (b) of 6LMFP·LVP/C between 2.0 and 4.8 V.

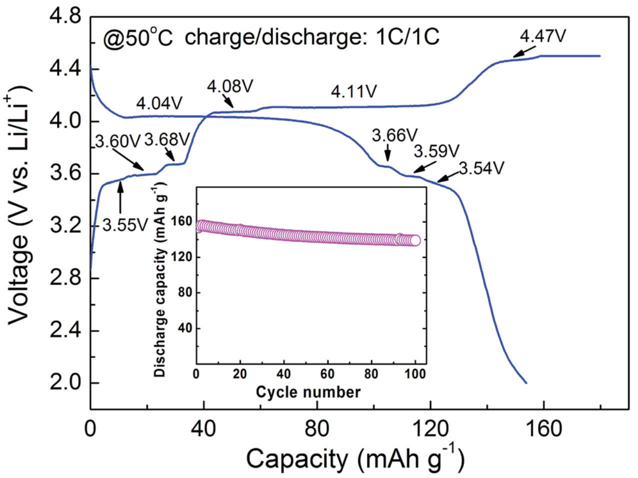

Fig. 7 Charge–discharge curve and cycle life (inset) of 6LMFP·LVP/C at 50 °C.

Fig. 9 shows the AC impedance spectra of LMP/C, LMFP/C, and 6LMFP·LVP/C electrodes at the fully discharged state after 100 cycles. All the spectra present a depressed semicircle in

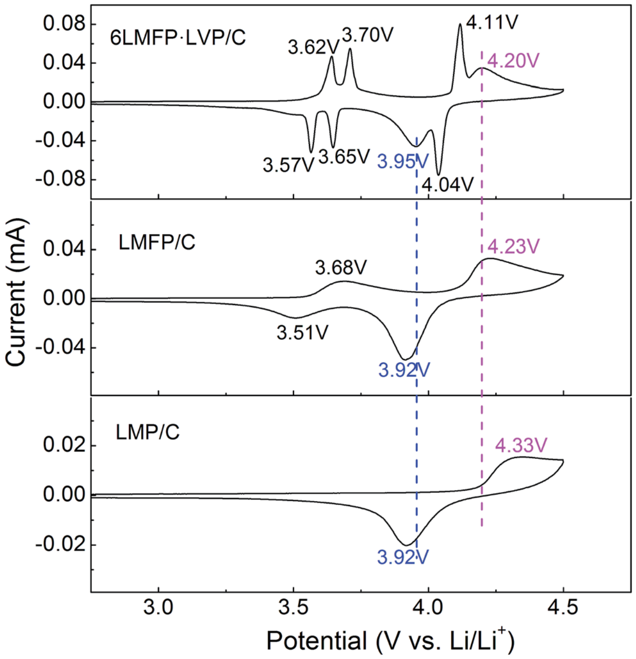

Fig. 8 CV curves of the LMP/C, LMFP/C, and 6LMFP·LVP/C electrodes.

the high-medium frequency region, corresponding to the charge-transfer impedance at the electrode/electrolyte interface, and a straight line in the low frequency region, relating to the Li^+ diffusion in the electrode material. The slope of the straight line is proportional to the Li^+ diffusion coefficient.[13,42] By comparing the diameter of the semicircles and the slope of the straight lines, it was found that 6LMFP·LVP/C exhibits smaller interface impedance and much faster Li^+ diffusion than LMFP/C and LMP/C. This demonstrates that the electronic and ionic conductivity of 6LMFP·LVP/C are better than those of LMFP/C and LMP/C and also clarifies the fast rate capability of 6LMFP·LVP/C.

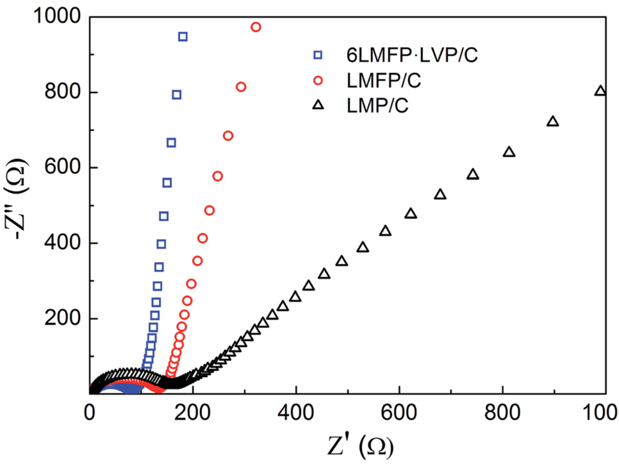

Fig. 9 EIS spectra of the LMP/C, LMFP/C, and 6LMFP·LVP/C electrodes after 100 cycles.

4. Conclusions

The $6LiMn_{0.8}Fe_{0.2}PO_4 \cdot Li_3V_2(PO_4)_3/C$ composite with the size of *ca.* 100–150 nm was successfully synthesized *via* a surfactant-assisted solid-state method employing lauric acid as a surfactant and carbon source. The use of lauric acid is beneficial for the fabrication of uniform nanoparticles with high dispersion. XRD and EDS mapping illustrate that the composite consists of $LiMn_{0.8}Fe_{0.2}PO_4$ and $Li_3V_2(PO_4)_3$ phases, and the $Li_3V_2(PO_4)_3$ phase uniformly diffuses into the $LiMn_{0.8}Fe_{0.2}PO_4$ matrix. The $6LiMn_{0.8}Fe_{0.2}PO_4 \cdot Li_3V_2(PO_4)_3/C$ composite exhibits much higher specific capacity and better rate capability than the individual $LiMn_{0.8}Fe_{0.2}PO_4/C$ and $LiMnPO_4/C$. The enhanced electrochemical performance of the multiphase composite demonstrates its use as a promising cathode material for high-power lithium ion batteries.

Acknowledgements

This work was supported by the National Natural Science Foundation of China (No. 21401061), Provincial Natural Science Research Foundation of Anhui Universities, China (No. KJ2015A332 and KJ2014A224), Innovation Team of Design and Application of Advanced Energetic Materials and the Key project of Anhui Universities support program for Outstanding Youth, China (No. gxyqZD2016111), Natural Science Foundation of Anhui Province, China (No. 1308085QB41), and the Henan Joint Funds of the National Natural Science Foundation of China (U1504532).

References

1 S. M. Oh, S. W. Oh, C. S. Yoon, B. Scrosati, K. Amine and Y. K. Sun, *Adv. Funct. Mater.*, 2010, **20**, 3260–3265.
2 T. Drezen, N.-H. Kwon, P. Bowen, I. Teerlinck, M. Isono and I. Exnar, *J. Power Sources*, 2007, **174**, 949–953.
3 C. Hu, H. Yi, H. Fang, B. Yang, Y. Yao, W. Ma and Y. Dai, *Electrochem. Commun.*, 2010, **12**, 1784–1787.
4 J. Xiong, Y. Wang, Y. Wang and J. Zhang, *Ceram. Int.*, 2016, **42**, 9018–9024.
5 S. Novikova, S. Yaroslavtsev, V. Rusakov, A. Chekannikov, T. Kulova, A. Skundin and A. Yaroslavtsev, *J. Power Sources*, 2015, **300**, 444–452.
6 Y. Hong, Z. Tang, Z. Hong and Z. Zhang, *J. Power Sources*, 2014, **248**, 655–659.
7 S. Li, Z. Su, A. Muslim, X. Jiang and X. Wang, *Ceram. Int.*, 2015, **41**, 11132–11135.
8 R. V. Hagen, H. Lorrmann, K.-C. Möller and S. Mathur, *Adv. Energy Mater.*, 2012, **2**, 553–559.
9 L. Chen, Y.-Q. Yuan, X. Feng and M.-W. Li, *J. Power Sources*, 2012, **214**, 344–350.
10 S.-Y. Yan, C.-Y. Wang, R.-M. Gu, S. Sun and M.-W. Li, *J. Alloys Compd.*, 2015, **628**, 471–479.
11 F. Ye, L. Wang, X. He, M. Fang, Z. Dai, J. Wang, C. Huang, F. Lian, J. Wang, G. Tian and M. Ouyang, *J. Power Sources*, 2014, **253**, 143–149.

12 P. Zuo, G. Cheng, L. Wang, Y. Ma, C. Du, X. Cheng, Z. Wang and G. Yin, *J. Power Sources*, 2013, **243**, 872–879.

13 B. Z. Li, Y. Wang, L. Xue, X. P. Li and W. S. Li, *J. Power Sources*, 2013, **232**, 12–16.

14 L. Yang, Y. Xia, L. Qin, G. Yuan, B. Qiu, J. Shi and Z. Liu, *J. Power Sources*, 2016, **304**, 293–300.

15 L. Yang, Y. Xia, X. Fan, L. Qin, B. Qiu and Z. Liu, *Electrochim. Acta*, 2016, **191**, 200–206.

16 Q.-Q. Zou, G.-N. Zhu and Y.-Y. Xia, *J. Power Sources*, 2012, **206**, 222–229.

17 J. Liu, W. Liao and A. Yu, *J. Alloys Compd.*, 2014, **587**, 133–137.

18 Y. P. Huang, T. Tao, Z. Chen, W. Han, Y. Wu, C. Kuang, S. Zhou and Y. Chen, *J. Mater. Chem. A*, 2014, **2**, 18831–18837.

19 C. Xu, L. Li, F. Qiu, C. An, Y. Xu, Y. Wang, Y. Wang, L. Jiao and H. Yuan, *J. Energy Chem.*, 2014, **23**, 397–402.

20 Z.-X. Chi, W. Zhang, X.-S. Wang, F.-Q. Cheng, J.-T. Chen, A.-M. Cao and L.-J. Wan, *J. Mater. Chem. A*, 2014, **2**, 17359–17365.

21 Y. Mi, P. Gao, W. Liu, W. Zhang and H. Zhou, *J. Power Sources*, 2014, **267**, 459–468.

22 W. Liu, P. Gao, Y. Mi, J. Chen, H. Zhou and X. Zhang, *J. Mater. Chem. A*, 2013, **1**, 2411–2417.

23 X. Yang, Y. Mi, W. Zhang, B. Wu and H. Zhou, *J. Power Sources*, 2015, **275**, 823–830.

24 W. Yang, Y. Bi, Y. Qin, Y. Liu, X. Zhang, B. Yang, Q. Wu, D. Wang and S. Shi, *J. Power Sources*, 2015, **275**, 785–791.

25 W. Xiang, E.-H. Wang, M.-Z. Chen, H.-H. Shen, S.-L. Chou, H. Chen, X.-D. Guo, B.-H. Zhong and X. Wang, *Electrochim. Acta*, 2015, **178**, 353–360.

26 C. Gao, H. Liu, G. Liu, J. Zhang and W. Wang, *Mater. Sci. Eng., B*, 2013, **178**, 272–276.

27 Y. Guo, Y. Huang, D. Jia, X. Wang, N. Sharma, Z. Guo and X. Tang, *J. Power Sources*, 2014, **246**, 912–917.

28 J.-f. Zhang, C. Shen, B. Zhang, J.-c. Zheng, C.-l. Peng, X.-w. Wang, X.-b. Yuan, H. Li and G.-m. Chen, *J. Power Sources*, 2014, **267**, 227–234.

29 B. Zhang, X.-w. Wang and J.-f. Zhang, *RSC Adv.*, 2014, **4**, 49123–49127.

30 S. Li, Z. Su and X. Wang, *RSC Adv.*, 2015, **5**, 80170–80175.

31 F. Wang, J. Yang, Y. NuLi and J. Wang, *Electrochim. Acta*, 2013, **103**, 96–102.

32 C. Wang, Y. Bi, Y. Liu, Y. Qin, Y. Fang and D. Wang, *J. Power Sources*, 2014, **263**, 332–337.

33 S. Zhong, L. Wu, J. Zheng and J. Liu, *Powder Technol.*, 2012, **219**, 45–48.

34 L. Qin, Y. Xia, B. Qiu, H. Cao, Y. Liu and Z. Liu, *J. Power Sources*, 2013, **239**, 144–150.

35 L. Chen, B. Yan, H. Wang, X. Jiang and G. Yang, *J. Power Sources*, 2015, **287**, 316–322.

36 L. Wu, J. Lu, G. Wei, P. Wang, H. Ding, J. Zheng, X. Li and S. Zhong, *Electrochim. Acta*, 2014, **146**, 288–294.

37 X. Zhou, Y. Xie, Y. Deng, X. Qin and G. Chen, *J. Mater. Chem. A*, 2015, **3**, 996–1004.

38 L. Zhang, Q. Qu, L. Zhang, J. Li and H. Zheng, *J. Mater. Chem. A*, 2014, **2**, 711–719.

39 M. Secchiaroli, F. Nobili, R. Tossici, G. Giuli and R. Marassi, *J. Power Sources*, 2015, **275**, 792–798.

40 Q. Li, F. Zheng, Y. Huang, X. Zhang, Q. Wu, D. Fu, J. Zhang, J. Yin and H. Wang, *J. Mater. Chem. A*, 2015, **3**, 2025–2035.

41 F. Zheng, C. Yang, X. Ji, D. Hu, Y. Chen and M. Liu, *J. Power Sources*, 2015, **288**, 337–344.

42 L. Mai, S. Li, Y. Dong, Y. Zhao, Y. Luo and H. Xu, *Nanoscale*, 2013, **5**, 4864–4869.